Inverse scattering solutions using low-coherence light

Renjie Zhou,[1,2] Taewoo Kim,[1] Lynford L. Goddard,[2] and Gabriel Popescu[1,2,*]

[1]*Quantitative Light Imaging Laboratory, Department of Electrical and Computer Engineering, Beckman Institute for Advanced Science & Technology, University of Illinois at Urbana-Champaign, Urbana, Illinois 61801, USA*

[2]*Micro and Nanotechnology Laboratory, Department of Electrical and Computer Engineering, University of Illinois at Urbana—Champaign, Urbana, Illinois 61801, USA*

**Corresponding author: gpopescu@illinois.edu*

Received April 21, 2014; revised June 23, 2014; accepted June 23, 2014; posted June 24, 2014 (Doc. ID 210563); published July 28, 2014

We present a new wave-vector-space approach for solving inverse scattering problems. In our formulation, the theories for diffraction tomography and coherence gating are combined to explain 3D reconstruction with low-coherence light. Specifically, we apply this method to solve the scattering problem with broadband fields for transmission and reflection measurements. Our results can be applied to any interferometric measurements with low-coherence light, including optical coherence tomography, angle-resolved low-coherence interferometry, and white-light diffraction tomography.

OCIS codes: (050.1960) Diffraction theory; (110.6955) Tomographic imaging; (180.1655) Coherence tomography; (180.3170) Interference microscopy; (170.4500) Optical coherence tomography.

http://dx.doi.org/10.1364/OL.39.004494

X-ray diffraction emerged in the early twentieth century as a method to infer the 3D structure of crystals [1]. Much of our current knowledge of crystals and protein structures is the result of solving the inverse scattering problem using x rays as the interrogating radiation [2,3]. It is known that, in x-ray experiments, one only has access to the *intensity* of the field. The missing *phase* information associated with the scattered field can lead to nonunique solutions in the reconstructed sample structure (see, for example, p. 304 in [4]). This obstacle is known in the x-ray community as "the phase problem."

In the optical regime, on the other hand, recording the phase information is quite practical, as Gabor first demonstrated in 1948 [5]. In 1969, Wolf reported a theoretical method for reconstructing the 3D structure of transparent objects from holographic measurements [6]. Such reconstruction, referred to as optical diffraction tomography (ODT), based on the first-order Born approximation, is most useful in biology, as unlabeled live cells are typically transparent to visible light [7–11]. Yet, 45 years after Wolf's paper, there is no commercial instrument that can provide 3D imaging of unlabeled live cells.

OCT, which is essentially spatially resolved low-coherence interferometry (LCI), was first demonstrated in 1991 as a label-free 3D imaging method for deep-tissue imaging [12]. OCT is an amplitude technique, which uses the narrow temporal cross-correlation function between the sample and reference fields to achieve axial sectioning, even with close to zero numerical aperture (NA) optics. Izatt *et al.* used the time derivatives of the phase (frequency shifts) to generate Doppler imaging [13]. The combination of OCT and ODT was not demonstrated until much later [14–16]. Ralston *et al.* showed that using the phase information in OCT measurements allows for solving the scattering inverse problem, which, in turn, can be used for reconstructing the 3D distribution of the tissue scattering potential with spatially invariant resolution [15,16]. Villiger and Lasser presented image formation in OCT using a coherent transfer function approach [17].

Very recently, ODT was implemented with white-light illumination in high NA imaging. This approach, called white-light diffraction tomography (WDT), shares the coherence gating principle of OCT, while measuring the signal in transmission [18]. WDT can be realized in any quantitative phase imaging (QPI) system [19–22]. Unlike OCT, the numerical aperture of the objective is crucial in achieving sectioning in WDT. With this method, 3D imaging of unlabeled live cells with submicrometer resolution in all three directions has been demonstrated. Furthermore, WDT presents an efficient and accurate way of solving the wave equation in the wave-vector space, rather than using the traditional Green's function approach. In this Letter, we apply this wave-vector-space method for solving inverse scattering under the Fresnel approximation in the time and Fourier domains. This inverse scattering solution can then be used for 3D reconstruction from OCT and LCI measurements, which typically deploy low NA systems suitable for the Fresnel approximation. Furthermore, the solution is physically interpreted on the Ewald sphere. We also provide analytical solutions for the time-domain reconstructions, which can be used for 3D imaging by scanning the optical pathlength delay between the reference and sample fields.

Figure 1 shows a schematic of the scattering problem. A plane wave U_i is incident on a transparent object, described by the scattering potential, χ, which perturbs U_i. The perturbations are carried by the scattering field U_s, both in the forward and backward scattering semi-space, represented by U_f and U_b, respectively. By interfering the scattered field with a reference field, we can measure the interference signal, which contains the phase information and, thus, the object's structure.

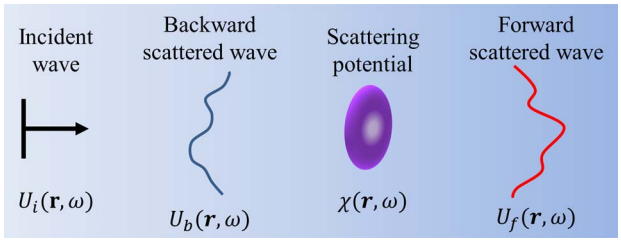

Fig. 1. Schematic of the scattering problem.

We start the mathematical formulation with the Helmholtz equation, describing the total field distribution in space and frequency:

$$\nabla^2 U(\boldsymbol{r},\omega) + n^2(\boldsymbol{r})\beta_0^2(\omega)U(\boldsymbol{r},\omega) = 0, \tag{1}$$

where $\beta_0(\omega) = \omega/c$ is the wavenumber or the propagation constant in vacuum. The total field $U(\mathbf{r},\omega)$ can be written as a sum, $U(\mathbf{r},\omega) = U_i(\mathbf{r},\omega) + U_s(\mathbf{r},\omega)$, where $U_i(\mathbf{r},\omega)$ is the incident field, and $U_s(\mathbf{r},\omega)$ is the scattered field. Since the incident field $U_i(\mathbf{r},\omega)$ satisfies the homogeneous wave equation, Eq. (1) can be reduced to

$$\nabla^2 U_s(\mathbf{r},\omega) + \beta^2(\omega)U_s(\mathbf{r},\omega) = -\beta_o^2(\omega)\chi(\mathbf{r})U(\mathbf{r},\omega), \tag{2}$$

where $\beta(\omega) = \bar{n}\beta_0(\omega)$ is the wavenumber in the medium, $\bar{n} = \langle n(\mathbf{r})\rangle$ is the spatially averaged refractive index, and $\chi(\mathbf{r},\omega) = n^2(\mathbf{r},\omega) - \bar{n}^2(\omega)$ is the scattering potential, the quantity of interest in this Letter. Unlabeled cells are optically thin due to their small size and refractive index variations. Therefore, most of the light goes under single forward scattering, such that the first-order Born approximation applies as well. ODT, for example, is based on the first-order Born approximation and correctly reconstructs unlabeled cell structures [7–11]. Under the first-order Born approximation, we have $|U_s(\mathbf{r},\omega)| \ll |U_i(\mathbf{r},\omega)|$. We assume the incident field is uniform over the field of view, which allows us to model it as a plane wave (the description can be generalized to an arbitrary incident field, as shown in [23]). Therefore, on the right hand side of Eq. (2), $U(\mathbf{r},\omega) \simeq U_i(\mathbf{r},\omega) \simeq A(\omega)e^{i\beta(\omega)z}$. By performing the Fourier transform (FT) of Eq. (2) with respect to $\mathbf{r}$, we obtain the scattered field solution in the wave-vector space as [18,23]

$$U_s(\mathbf{k},\omega) = -\beta_0^2(\omega)A(\omega)\chi[\mathbf{k}_\perp, k_z - \beta(\omega)]\frac{1}{2q}\left(\frac{1}{k_z - q} - \frac{1}{k_z + q}\right), \tag{3}$$

where we define $q = \sqrt{\beta^2(\omega) - k_\perp^2}$ and $k_\perp^2 = k_x^2 + k_y^2$. Considering either forward scattering, $1/(k_z - q)$, or backward scattering, $1/(k_z + q)$, and taking the inverse FT with respect to k_z, we have

$$U_s(\boldsymbol{k}_\perp, z, \omega) = \mp\frac{\beta_o^2(\omega)}{2}A(\omega)\left\{\chi(\boldsymbol{k}_\perp, z)e^{i\beta(\omega)z}\circledv_z \frac{e^{\pm iqz}}{q}\right\}, \tag{4}$$

where $\circledv_z$ denotes 1D convolution over z. Using the definition, the convolution in Eq. (4) is evaluated as $[\chi(k_\perp, z)e^{i\beta(\omega)z}]\circledv_z e^{iqz} = e^{iqz}\chi[\boldsymbol{k}_\perp, q - \beta(\omega)]$. Therefore, we can immediately evaluate Eq. (4) as

$$U_f(\boldsymbol{k}_\perp, z, \omega) = -\frac{\beta_o^2(\omega)A(\omega)e^{iqz}}{2q}\chi[\boldsymbol{k}_\perp, q - \beta(\omega)], \tag{5a}$$

$$U_b(\boldsymbol{k}_\perp, z, \omega) = \frac{\beta_o^2(\omega)A(\omega)e^{-iqz}}{2q}\chi[\boldsymbol{k}_\perp, -q - \beta(\omega)], \tag{5b}$$

where U_f and U_b are the forward and backward scattered fields, respectively. Note that, although we assume a dispersionless medium, the scattered fields have strong dependence on the optical frequency. In most interferometric microscopy experiments, the measured signal is the cross correlation between the scattered and reference fields. Under the first-order Born approximation, where the reference field equals the incident field, the cross-spectral density can be written as [23]

$$W(\boldsymbol{k}_\perp, z, \omega) = U_s(\boldsymbol{k}_\perp, z, \omega)U_r^*(z_R, \omega), \tag{6}$$

where $U_r(z_R,\omega) = A(\omega)e^{i\beta(\omega)\cdot z_R}$, and z_R is the propagation distance of the reference beam with respect to $z = 0$. The coordinate system is fixed once the scattering potential is specifically defined. Thus, the general solutions to the inverse scattering are

$$\chi(\boldsymbol{k}_\perp, q - \beta) = -\frac{2qW_f(\boldsymbol{k}_\perp, z, \beta)}{\beta_o^2 S(\beta)}e^{-i(qz - \beta\cdot z_R)}, \tag{7a}$$

$$\chi(\boldsymbol{k}_\perp, -q - \beta) = \frac{2qW_b(\boldsymbol{k}_\perp, z, \beta)}{\beta_o^2 S(\beta)}e^{i(qz + \beta\cdot z_R)}, \tag{7b}$$

where W_f and W_b are the forward and backward measured fields, and $S(\beta) = |A(\beta)|^2$ is the power spectrum of the incident field. Note that, in experiments, we usually measure $S(\lambda)$ [18]. Therefore, in order to obtain $S(\beta)$, we need to consider a Jacobian transformation, i.e., $S(\beta) = -\lambda^2 S(\lambda)/(2\pi\bar{n})$. If $W_f(\lambda)$ and $W_b(\lambda)$ are measured, as in Fourier-domain OCT, the Jacobian also is necessary in order to transform W to the β domain.

There are several significant implications of Eq. (7). First, it establishes the 3D reconstruction model for ODT. As shown in the scattering potential χ, the object sectioning is determined by $q - \beta$ in transmission and $-q - \beta$ in reflection. In other words, the 3D reconstruction can be achieved by scanning the incident plane wave angle, $q = \sqrt{\beta^2 - k_\perp^2}$, or scanning the frequency, β. Notice that, to numerically reconstruct the 3D object, a resampling of the axial frequency k_z as $k_z = q - \beta = \sqrt{\beta^2 - k_\perp^2} - \beta$ is necessary. As demonstrated previously, regularization or sparse deconvolution methods can be used to obtain uniform object reconstruction [16,18,24]. In particular, Eq. (7b) can be used for high-resolution Fourier-domain OCT, without the far-field approximation used in [16]. Finally, Eq. (7) also describes the scattering measurement in angle-resolved LCI (aLCI) for determining depth-resolved angular scattering from tissues, without the need for the Mie theory assumption (note that $\mathbf{k}_\perp$ is proportional to the sine of the scattering angle) [25,26].

In order to integrate the forward and backward scattered signal in Eq. (7), with respect to frequency β, and obtain the time-domain solution, we use the Fresnel approximation. For an imaging system under this approximation, using the Taylor expansion, we have

$$q = \sqrt{\beta^2 - k_\perp^2} \approx \beta\left(1 - \frac{k_\perp^2}{2\beta^2}\right), \quad \text{thus,}$$
$$\beta^2/q \approx \beta\left(1 + \frac{k_\perp^2}{2\beta^2}\right). \tag{8}$$

Therefore, the solutions to 3D object reconstruction using forward and backward scattering become

$$\chi\left(\boldsymbol{k}_\perp, \frac{k_\perp^2}{2\beta}\right) \approx -\frac{2\bar{n}^2 W_f(\boldsymbol{k}_\perp, z, \beta)}{\beta S(\beta)} e^{-i\beta(z-z_R)} e^{i\frac{k_\perp^2 z}{2\beta}}, \tag{9a}$$

$$\chi\left(\boldsymbol{k}_\perp, \frac{k_\perp^2}{2\beta} - 2\beta\right) \approx \frac{2\bar{n}^2 W_b(\boldsymbol{k}_\perp, z, \beta)}{\beta S(\beta)} e^{i\beta(z+z_R)} e^{-i\frac{k_\perp^2 z}{2\beta}}. \tag{9b}$$

In the following, we provide a physical interpretation for Eq. (9). In elastic scattering, we have the dispersion relation $|\mathbf{k}_s| = |\mathbf{k}_i| = \beta$, where $\mathbf{k}_s = \mathbf{k}_\perp + \mathbf{k}_z$ and $\mathbf{k}_i$ are the scattering and incident wave vectors, respectively. Figure 2(a) shows a cross section of the Ewald sphere of radius β, which explains the sectioning effect. In the right triangle ABC [Fig. 2(a)], the length of the segments BC, AC, and BD is related to the wave vectors as $BC = |\mathbf{p}|$, $AC = 2\beta$ and $BD = |\mathbf{k}_\perp|$, where $\mathbf{p} = \mathbf{k}_s - \mathbf{k}_i$ is the momentum transfer wave vector. Using the similarities of triangles ABC and BCD, $BD^2 = AD \cdot DC$, meaning that

$$k_\perp^2 = |\beta + k_z||\beta - k_z| \approx 2\beta|\beta - k_z|, \tag{10a}$$

which implies

$$|\beta - k_z| = \frac{k_\perp^2}{2\beta}. \tag{10b}$$

$|\beta - k_z|$ is the axial projection of $\mathbf{p}$, $p_z = k_\perp^2/2\beta$, whose spread determines the sectioning in z. Note that this projection appears explicitly in Eq. (9a) through the scattering potential, $\chi(\boldsymbol{k}_\perp, k_\perp^2/2\beta)$. This is expected, as measuring the scattered field at a scattering wave vector provides a single spatial frequency of the object. Considering the wave-vector geometry described in Fig. 2(b), we find that, in backward scattering, the momentum transfer wave vector has a projection of $p_z = -2\beta + k_\perp^2/2\beta$, which also appears in Eq. (9b). From the comparison of the two wave-vector geometries, we see that backscattering has a better sectioning effect due to the longer axial projection coming from 2β.

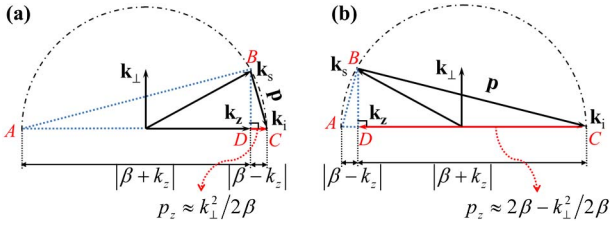

Fig. 2. Interpretation of sectioning effects on the Ewald sphere. (a) Forward scattering wave-vector relations. (b) Backward scattering wave-vector relations.

Next, we derive the time-domain tomographic reconstruction model in transmission and reflection geometry. At $z = z_R$, the forward scattering interference signal W_f, described in Eq. (9a), becomes

$$W_f(\boldsymbol{k}_\perp, z, \beta) \approx -\frac{1}{2\bar{n}^2}\beta S(\beta)\chi\left(\boldsymbol{k}_\perp, \frac{k_\perp^2}{2\beta}\right) e^{-i\frac{k_\perp^2 z}{2\beta}}. \tag{11}$$

In order to obtain the time-domain solution, we perform the inverse FT over $\Omega = k_\perp^2/2\beta$, which ensures proper resampling of k_z. As $\beta = k_\perp^2/2\Omega$, the Jacobian transformation relates the power spectrum $S(\beta)$ and $S(\Omega)$:

$$S(\beta) = S(\Omega)\frac{d\Omega}{d\beta} = -S(\Omega)\frac{k_\perp^2}{2\beta^2} = -\frac{2\Omega^2 S(\Omega)}{k_\perp^2}. \tag{12}$$

Note that Ω has a unit of m^{-1}, and its conjugate variable is $c\tau$, with c the speed of light in the medium and τ the time delay between the reference and object field. Using the new variable, Eq. (11) becomes

$$W_f(\boldsymbol{k}_\perp, z, \Omega) \approx \frac{1}{2\bar{n}^2}\Omega S(\Omega)\chi(\boldsymbol{k}_\perp, \Omega)e^{-i\Omega z}. \tag{13}$$

Taking the inverse FT of Eq. (13) with respect to Ω, and using the FT property, $\Omega S(\Omega) \overset{\mathbb{F}}{\leftrightarrow} -i\partial\Gamma(c\tau)/\partial c\tau$, we obtain

$$\Gamma_f(\boldsymbol{k}_\perp, z, c\tau) = -\frac{i}{2\bar{n}^2}\frac{\partial\Gamma_0(\boldsymbol{k}_\perp, c\tau)}{\partial(c\tau)} \circledV_{c\tau} \chi(\boldsymbol{k}_\perp, c\tau - z), \tag{14}$$

where Γ_0 is the temporal autocorrelation function of the source field, defined as

$$\Gamma_0(\boldsymbol{k}_\perp, c\tau) = FT^{-1}\{S(\Omega)\} = |\Gamma_0(\boldsymbol{k}_\perp, c\tau)|e^{i\bar{\Omega}c\tau}. \tag{15}$$

For simplicity, here we assume a symmetric optical spectrum. Under the slowly varying envelope approximation for Γ_0,

$$\frac{\partial\Gamma_0(\boldsymbol{k}_\perp, c\tau)}{\partial(c\tau)} = i\bar{\Omega}\Gamma_0(\boldsymbol{k}_\perp, c\tau) + \frac{\partial|\Gamma_0(c\tau)|}{\partial(c\tau)}e^{i\bar{\Omega}c\tau}$$
$$\approx i\bar{\Omega}\Gamma_0(\boldsymbol{k}_\perp, c\tau). \tag{16}$$

With this approximation, the temporal cross-correlation function simplifies to

$$\Gamma_f(\boldsymbol{k}_\perp, z, c\tau) \approx \frac{i}{2\bar{n}^2}\bar{\Omega}\Gamma_0(\boldsymbol{k}_\perp, c\tau) \circledV_{c\tau} \chi(\boldsymbol{k}_\perp, c\tau - z). \tag{17}$$

Equation (17) provides the reconstruction model for a transmission measurement with LCI. This is analogous to a transmission OCT. This equation indicates that the axial reconstruction can be obtained by simply scanning the delay $c\tau$ or by translating the object in z. As a result of the convolution operation, the axial resolution is given by the width of Γ_0, i.e., the *coherence length* of the field. If the source Γ_0 is measured, deconvolution or regularization methods also can be used to improve the axial reconstruction of χ.

In backscattering, for $z = z_R$, Eq. (9b) becomes

$$W_b(\boldsymbol{k}_\perp, z, \beta) \approx \frac{1}{2\bar{n}^2}\beta S(\beta)\chi\left(\boldsymbol{k}_\perp, \frac{k_\perp^2}{2\beta} - 2\beta\right)e^{i\left(\frac{k_\perp^2}{2\beta}-2\beta\right)z}. \quad (18)$$

In order to obtain the time-domain reconstruction model, we define $Q = k_\perp^2/2\beta - 2\beta$. Thus, $\beta = (-Q + \sqrt{Q^2 + 4k_\perp^2})/4$ (the negative solution for β is unphysical). Again, considering the Jacobian transformation,

$$S(\beta) = S(Q)\frac{dQ}{d\beta} = S(Q)\frac{4\sqrt{Q^2 + 4k_\perp^2}}{Q - \sqrt{Q^2 + 4k_\perp^2}}, \quad (19)$$

Eq. (18) becomes

$$W_b(\boldsymbol{k}_\perp, z, \beta) \approx -\frac{2}{\bar{n}^2}\sqrt{Q^2 + 4k_\perp^2}S(Q)\chi(\boldsymbol{k}_\perp, Q)e^{iQz}. \quad (20)$$

When $k_\perp \ll |Q|$, under the Fresnel approximation, we can use the Taylor expansion by keeping the linear and quadratic terms, $\sqrt{Q^2 + 4k_\perp^2} \approx Q + 2k_\perp^2/Q$. Further, under the Fraunhofer approximation, only the linear term is kept, $Q + 2k_\perp^2/Q \approx Q$; thus, Eq. (20) becomes

$$W_b(\boldsymbol{k}_\perp, z, \beta) \approx \frac{2}{\bar{n}^2}QS(Q)\chi(\boldsymbol{k}_\perp, Q)e^{iQz}. \quad (21)$$

This equation resembles Eq. (13) and can be used to obtain the temporal correlation function in Eq. (17) as well. However, the meaning of the variable Q, which determines that the sectioning is different than Ω, Q introduces a better sectioning effect due to the extra -2β factor [15,16]. From Eq. (20), we also see that light scattering associated with the scattering vector $\mathbf{k}_\perp$ affects the reconstruction in time-domain OCT.

In summary, we presented a new way of solving the inverse scattering problem in the wave-vector space [Eqs. (7a) and (7b)], without far-field approximations. This method provides a theoretical foundation for achieving high-resolution Fourier-domain 3D reconstructions. We applied our method for systems under the Fresnel approximation and formulated the Fourier- and time-domain 3D reconstruction models in transmission and reflection. The models are expected to improve experimental results by achieving spatially invariant high-resolution reconstruction with low-coherence light. Aside from solving inverse scattering problems, we envision solving wave equations in the wave-vector space, i.e., bypassing the Green's function, to be widely used in the future for many other optical problems.

As quantitative phase imaging and light scattering are now merged into a single discipline, we anticipate that better understanding of light-tissue interaction will emerge. In particular, due to lack of better tools for studying tissue scattering, researchers have assumed for a long time the size distribution of spheres, scattering independently and, thus, obeying Mie theory. Today, QPI of thin tissues is much more informative, revealing strong spatial correlations in unlabeled tissues and connecting these to the scattering of the bulk [27].

This work was supported by NSF grants: CBET 0939511 (to GP and TK), CBET-1040461 MRI (to GP and LLG), and by the Beckman Foundation graduate fellowship (to RZ).

References

1. W. L. Bragg, Proc. R. Soc. A **89**, 248 (1913).
2. J. Als-Nielsen and D. McMorrow, *Elements of Modern X-ray Physics* (Wiley, 2001).
3. A. C. Kak and M. Slaney, *Principles of Computerized Tomographic Imaging* (Society for Industrial and Applied Mathematics, 2001).
4. E. Wolf, *Advances in Imaging and Electron Physics*, P. W. E. Hawkes, ed. (Academic, 2011).
5. D. Gabor, Nature **161**, 777 (1948).
6. E. Wolf, Opt. Commun. **1**, 153 (1969).
7. R. Fiolka, K. Wicker, R. Heintzmann, and A. Stemmer, Opt. Express **17**, 12407 (2009).
8. O. Haeberle, K. Belkebir, H. Giovaninni, and A. Sentenac, J. Mod. Opt. **57**, 686 (2010).
9. W. Choi, C. Fang-Yen, K. Badizadegan, S. Oh, N. Lue, R. R. Dasari, and M. S. Feld, Nat. Methods **4**, 717 (2007).
10. Y. Sung, W. Choi, N. Lue, R. R. Dasari, and Z. Yaqoob, PloS ONE **7**, e49502 (2012).
11. Y. Cotte, F. Toy, P. Jourdain, N. Pavillon, D. Boss, P. Magistretti, P. Marquet, and C. Depeursinge, Nat. Photonics **7**, 113 (2013).
12. D. Huang, E. A. Swanson, C. P. Lin, J. S. Schuman, W. G. Stinson, W. Chang, M. R. Hee, T. Flotte, K. Gregory, C. A. Puliafito, and J. G. Fujimoto, Science **254**, 1178 (1991).
13. J. A. Izatt, M. D. Kulkami, S. Yazdanfar, J. K. Barton, and A. J. Welch, Opt. Lett. **22**, 1439 (1997).
14. A. F. Fercher, J. Biomed. Opt. **1**, 157 (1996).
15. T. S. Ralston, D. L. Marks, P. S. Carney, and S. A. Boppart, J. Opt. Soc. Am. A **23**, 1027 (2006).
16. T. S. Ralston, D. L. Marks, P. S. Carney, and S. A. Boppart, Nat. Phys. **3**, 129 (2007).
17. M. Villiger and T. Lasser, J. Opt. Soc. Am. A **27**, 2216 (2010).
18. T. Kim, R. Zhou, M. Mir, S. D. Babacan, P. S. Carney, L. L. Goddard, and G. Popescu, Nat. Photonics **8**, 256 (2014).
19. Z. Wang, L. J. Millet, M. Mir, H. Ding, S. Unarunotai, J. A. Rogers, M. U. Gillette, and G. Popescu, Opt. Express **19**, 1016 (2011).
20. G. Popescu, T. Ikeda, R. R. Dasari, and M. S. Feld, Opt. Lett. **31**, 775 (2006).
21. B. Bhaduri, C. Edwards, H. Pham, R. Zhou, G. Popescu, and L. L. Goddard, Adv. Opt. Photon. **6**, 57 (2014).
22. G. Popescu, *Quantitative Phase Imaging of Cells and Tissues* (McGraw-Hill, 2011).
23. T. Kim, R. Zhu, T. H. Nguyen, R. Zhou, C. Edwards, L. L. Goddard, and G. Popescu, Opt. Express **21**, 20806 (2013).
24. Y. Yasuno, J. Sugisaka, Y. Sando, Y. Nakamura, S. Makita, M. Itoh, and T. Yatagai, Opt. Express **14**, 1006 (2006).
25. A. Wax, C. H. Yang, V. Backman, M. Kalashnikov, R. R. Dasari, and M. S. Feld, J. Opt. Soc. Am. A **19**, 737 (2002).
26. J. W. Pyhtila and A. Wax, Opt. Express **12**, 6178 (2004).
27. R. Zhu, S. Sridharan, K. Tangella, A. Balla, and G. Popescu, Opt. Lett. **36**, 4209 (2011).